ADVANCED ENERGY MATERIALS
www.advenergymat.de

Gradient Structural and Compositional Design of Conductive MXene Aerogels for Stable Zn Metal Anodes

Yang Li, Zhenqian Pang, Awais Ghani, Joshua M. Little, Liping Wang, Haochen Yang, Yusheng Zhao, and Po-Yen Chen**

Aqueous rechargeable zinc-ion batteries (ZIBs) are a safe and low-cost energy storage technology. However, practical ZIB exploitation faces critical challenges in achieving stable Zn metal anodes, which suffer from hydrogen evolution reaction (HER) corrosion and Zn dendrite growth. To address these challenges, a Zn^{2+}-induced assembly process to fabricate $Ti_3C_2T_x$ MXene-reduced graphene oxide aerogels with ZnO crust layers on Zn plates (abbreviated as ZnO/MG aerogel–Zn) that serve as stable Zn metal anodes is reported. By applying a constant voltage to a Zn plate, Zn^{2+} is gradually released to ionically crosslink MG nanosheets. After spontaneous hydrolysis and freeze-drying, a crust layer composed of ZnO nanoparticles is in situ formed. Additionally, the gradient Zn—O/Zn—F profiles across the ZnO/MG aerogel can facilitate Zn^{2+} transport and collectively suppress HER, enabling fast electrochemical kinetics and dendrite-free Zn deposition. Symmetric cells with ZnO/MG aerogel–Zn electrodes present stable cycling for 1200 h at 10 mA cm^{-2}, and full cells achieve long lifespans at high rates (>500 cycles at 1.0 A g^{-1}). Combining the advantages of an insulating protective layer and a conductive structured host, the ZnO/MG aerogel–Zn electrode with gradient structures and compositions creates synergistic advances in stable Zn metal anodes.

1. Introduction

Aqueous rechargeable zinc-ion batteries (ZIBs) are a promising new generation of safe, low-cost, and environmentally friendly energy storage technology.[1–4] Zinc (Zn) metal serves as the anode of ZIB and involves a two-electron redox process, demonstrating a high theoretical energy capacity (820 mAh g^{-1}) and a low redox potential (−0.76 V vs standard hydrogen electrode).[5] However, using Zn metal anodes for commercial applications is still hampered by two long-lasting challenges. First, when hydrated Zn^{2+} transports to the surface of the Zn metal anode, hydrogen evolution reaction (HER) tends to corrode and passivate the anode, largely attenuating Zn metal utilization rates and sacrificing battery stability.[6–8] Second, if without any control manners, the deposition of Zn metal normally leads to severe dendrite growth and forms "dead Zn" phases.[7,9,10] These two challenges (i.e., HER corrosion and dendrite formation) ultimately limit the Coulombic efficiencies and cyclability of ZIBs, thus hindering their future commercial potential.

To improve the stability of Zn metal anodes, various approaches have been developed in the literature, such as optimization of electrolyte composition,[10–12] design of structured Zn metal anodes,[13,14] and deposition of artificial protective layers.[9,15] Among these approaches, the

Y. Li, J. M. Little, H. Yang, P.-Y. Chen
Department of Chemical and Biomolecular Engineering
University of Maryland
College Park, MD 20740, USA
E-mail: checp@umd.edu
Y. Li, P.-Y. Chen
Maryland Robotics Center
University of Maryland
College Park, MD 20742, USA

Z. Pang, A. Ghani
Department of Architecture
College of Civil Engineering and Architecture
Zhejiang University
Hangzhou 310027, China
Z. Pang, A. Ghani
Smart Materials for Architecture Research Lab
Innovation Center of Yangtze River Delta
Zhejiang University
Jiaxing 314100, China
L. Wang, Y. Zhao
Department of Physics
Southern University of Science and Technology
Shenzhen 518055, China
E-mail: zhaoys@sustech.edu.cn

The ORCID identification number(s) for the author(s) of this article can be found under https://doi.org/10.1002/aenm.202301557

DOI: 10.1002/aenm.202301557

deposition of protective layers on Zn metal anodes can prohibit direct electron transfer to aqueous electrolytes and effectively suppress HER corrosion. Normally, the protective layers are designed to be electronically insulative and zincophilic, such as ionically conductive polymers (ZIF-7 MOF,[16] acrylate copolymer,[17] PVDF–TiO_2[18]) and metal oxides (TiO_2,[19] $CaCO_3$,[20] Al_2O_3[21]), all of which have demonstrated to improve the stability of Zn metal anodes. However, one associated drawback is the increased charge transfer resistances at the electrolyte/anode interfaces, which slows down the reaction kinetics of reversible Zn deposition/stripping.[16,17,19–21] Thus, the reported ZIBs with protective layers were shown to perform well at relatively lower current densities (≤3.0 mA cm^{-2}). Another promising approach is to design 3D, hierarchically structured Zn metal anodes, including 3D carbon–Zn,[22,23] 3D Sn–Zn,[24] 3D Cu–Zn,[25] and 3D alloy–Zn anodes.[26–28] These structured Zn metal anodes have been demonstrated to guide Zn metal deposition and restrain dendrite formation by reducing localized charge densities and electric fields. Nonetheless, because the top surfaces of structured Zn metal anodes were still electrically conductive, active HER corrosion was promoted, thus decreasing the anode stability. To ensure long-term operations without sacrificing the reaction kinetics of Zn metal anodes, a better compositional and structural design is highly desired for Zn metal anodes.

Recently, a synergistic strategy has emerged to fabricate electrochemical electrodes with gradient structures, compositions, and/or electrical conductivities. The gradient electrode design has shown various advantageous effects on different metal anodes, including Li, Na, and Zn.[29,30] For example, by combining two or more different layers of functional materials, metal anodes with multilayer configurations have been developed, such as ZnO/carbon nanofiber–Li and Cu@PVDF/Cu/Cu@Ag–Li for Li metal anodes,[31,32] NiO/Ni/Ag host,[33] ZnF_2/CuZn–Zn,[34] PVDF/Sn–Zn,[35] and HfO_2/Zn_xHfO_y–Zn[36] for Zn metal anodes. However, these multilayer metal anodes suffered from large interfacial resistances and disordered electron/ion distributions.[31,33] Additionally, multi-step and complicated fabrication processes were typically required, including sputtering, electrospinning, and high-temperature calcination, limiting the scalability of anode manufacturing.[32,33,36] Furthermore, the fabrication of several gradient metal anodes was required to incorporate non-active metal foams, which inevitably sacrificed their energy densities.[31,33]

Herein, a facile Zn^{2+}-induced assembly process was reported to fabricate a conductive $Ti_3C_2T_x$ MXene–reduced graphene oxide (MG) aerogel, featuring a ZnO crust layer and gradient Zn–O/Zn–F distributions (named as ZnO/MG aerogel afterward). By applying a constant voltage on a Zn plate, Zn^{2+} was gradually released into the MG dispersion, and the MG nanosheets were ionically crosslinked into a Zn^{2+}–MG hydrogel. By immersing the Zn^{2+}–MG hydrogel in a water bath, ZnO nanoparticles were in situ synthesized on the hydrogel's surface via a spontaneous hydrolysis reaction. Followed by freeze-drying, a ZnO/MG aerogel with gradient structural and compositional design was produced, consisting of a conductive MXene framework and an insulative ZnO crust layer. With the ZnO crust layer, the ZnO/MG aerogel effectively suppressed the HER corrosion by stripping the water sheath of hydrated Zn^{2+}. Additionally, the gradient Zn–O/Zn–F profiles across the ZnO/MG aerogel facilitated Zn^{2+} transport, enabling fast electrochemical kinetics and dendrite-free Zn deposition. With structural and compositional gradients, the ZnO/MG aerogel electrode demonstrated superior Zn plating/stripping reversibility with an average Coulombic efficiency of 99.2% over 1600 cycles at a large current density of 80 mA cm^{-2}. Moreover, the symmetric cell using a pair of ZnO/MG aerogel electrodes on Zn plates (abbreviated as ZnO/MG aerogel–Zn) presented stable cycling performance for 1200 h at large current densities of 5 and 10 mA cm^{-2}. By further coupling the ZnO/MG aerogel–Zn anode with a MnO_2 cathode, the full cell achieved a long lifespan at high rates (>500 cycles at 1.0 A g^{-1}), showing capacity retention over 60.6%. By combining the advantages of both an insulative protective layer and a conductive structured anode, the ZnO/MG aerogel–Zn electrode with gradient structures, compositions, and conductivities creates synergistic advances in stable Zn metal anodes, producing high-performance ZIBs with long-term cycling and fast reaction kinetics.

2. Results and Discussion

2.1. Zn^{2+}-Induced Assembly of $Ti_3C_2T_x$ MXene-Reduced Graphene Oxide Aerogels with ZnO Crust Layers (ZnO/MG Aerogels)

$Ti_3C_2T_x$ MXene nanosheets were synthesized by etching Ti_3AlC_2 MAX crystals in the solution of hydrochloride acid (HCl) and lithium fluoride (LiF) followed by exfoliation, and the as-exfoliated MXene nanosheets were with the lateral flake size ranging from 500 to 1000 nm (transmission electron microscope image in Figure S1, Supporting Information). Also, graphene oxide (GO) nanosheets with larger flake sizes over several micrometers were obtained (Figure S2, Supporting Information).

Figure 1a presents the major steps for the fabrication of ZnO/MG aerogels, including 1) Zn^{2+}-induced gelation of MXene and GO nanosheets, 2) in situ formation of ZnO nanocrystals via spontaneous hydrolysis, and 3) creation of ZnO/MG aerogels via freeze drying. As shown in Figure 1b, the Zn^{2+}-induced gelation of MXene/GO nanosheets was conducted in a two-electrode configuration with a constant voltage of 50 mV, where a platinum plate and a Zn plate were used as the cathode and the anode, respectively, with the MXene/GO dispersion as the electrolyte. The purpose of incorporating GO nanosheets was to enhance the structural stability and mechanical strengths of ZnO/MG aerogels (Figure S3, Supporting Information),[37,38] and the optimal GO loading was determined to be 30 wt.%. As demonstrated in Figure S4 (Supporting Information) (cross-section SEM images) and Figure S5 (Supporting Information) (compressive stress–strain curves), the Zn^{2+}-induced MG aerogel (with 30 wt.% GO) exhibited horizontally aligned micropores with higher compressive stress of 83 kPa than the Zn^{2+}-induced MXene aerogel (without GO, 30 kPa) with irregularly shaped micropores. Upon the applied voltage, the Zn metal anode continued to get oxidized and release Zn^{2+} (Reaction 1), causing the Zn^{2+}-induced gelation of MXene/GO nanosheets on the surface of the Zn plate (Figure 1a, Step 1). At the cathode side, water received electrons

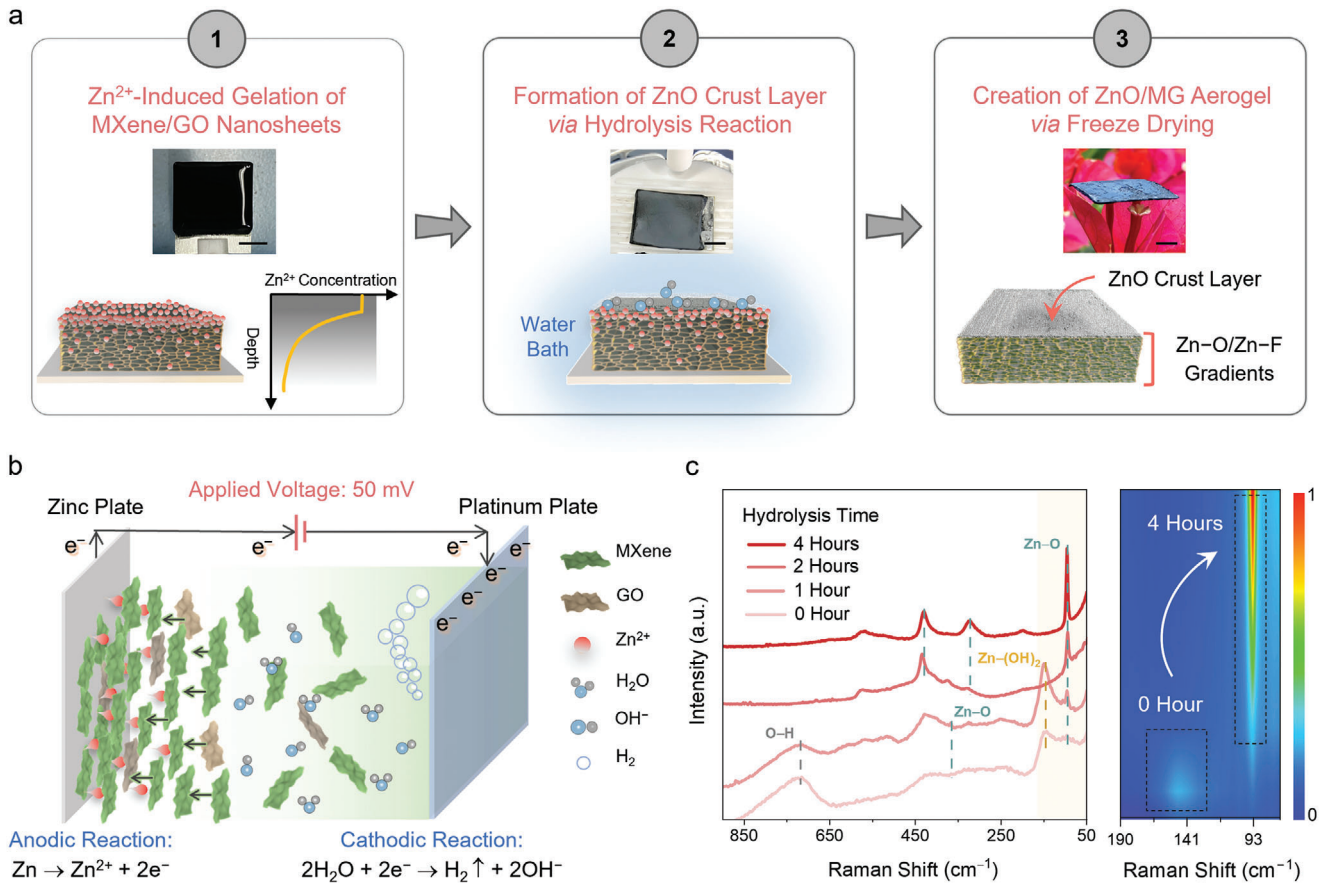

Figure 1. Zn^{2+}-induced assembly of ZnO/MG aerogels. a) Major steps for the fabrication of ZnO/MG aerogels: (1) Zn^{2+}-induced gelation of MXene and GO nanosheets, (2) in situ formation of ZnO nanocrystals via spontaneous hydrolysis, and (3) creation of ZnO/MG aerogel via freeze drying. Inset digital photographs (scale bar: 1.0 cm) include a Zn^{2+}–MG hydrogel (after Step 1), a ZnO/MG hydrogel after hydrolysis (after Step 2), and a lightweight ZnO/MG aerogel on flowers (after Step 3). b) Schematic illustration of Zn^{2+}-induced MXene/GO gelation process under a constant voltage of 50 mV. c) Raman spectra of Zn^{2+}–MG hydrogels at different hydrolysis intervals and the corresponding time-dependent contour map.

and underwent HER (Reaction 2),[39,40] and the HER-generated hydroxyl groups (OH^-) would migrate to the anode side.

$$\text{Anodic Reaction}: \quad Zn \rightarrow Zn^{2+} + 2e^- \tag{1}$$

$$\text{Cathodic Reaction}: \quad 2H_2O + 2e^- \rightarrow H_2\,(\text{gas}) + 2OH^- \tag{2}$$

Under the applied voltage, the Zn^{2+}–MG hydrogel exhibited a gradient distribution of Zn^{2+}, the concentration of which decreased from the hydrogel/electrolyte interface to the hydrogel/anode interface (the inset of Figure 1a, Step 1). As shown in Figure S6 (Supporting Information), the thickness of Zn^{2+}–MG hydrogel continually increased even after the applied voltage was cut off, as the Zn^{2+} gradient slowly got equilibrated by releasing Zn^{2+} at the hydrogel/electrolyte interface.

Next, the Zn^{2+}–MG hydrogel (on the Zn plate) was immersed into deionized (DI) water (Figure 1a, Step 2), during which Zn^{2+} continued to diffuse out and attracted OH^- to form $Zn(OH)_2$ at the hydrogel/water interface (the formation constant of $Zn(OH)_2$, $K = 2.8 \times 10^{16}$ at pH ≈7.0, Reaction 3).[41–43] As shown in the contour map of Raman spectra (the inset of Figure 1c), $Zn(OH)_2$ was immediately formed on the outer surface of Zn^{2+}–MG hydrogel (close to the water side), showing the representative peaks at 367 and 150 cm^{-1} (representing tetrahedron symmetric Zn–O stretching and Zn–$(OH)_2$ vibration modes).[42,44,45] Also, the broadband at 723 cm^{-1} represented the O–H liberation mode.[16,46]

$$Zn^{2+} + 2OH^- \rightarrow Zn(OH)_2 \tag{3}$$

$$Zn(OH)_2 \rightarrow ZnO \downarrow + H_2O \tag{4}$$

After 1 h, the as-formed $Zn(OH)_2$ phase started to decompose into ZnO nanoparticles ($\Delta G = -1.7$ kJ mol^{-1} at 25 °C, Reaction 4).[39,41,47–50] After 4 h, $Zn(OH)_2$ was fully transformed into ZnO nanoparticles, where the E_2^{low} phonon mode of ZnO was observed at 95.6 cm^{-1}.[51,52] Also, the existence of ZnO nanoparticles was confirmed by the digital photo (the inset of Figure 1a, Step 2 and Figure S7, Supporting Information) and the X-ray diffraction (XRD) patterns (**Figure 2**c). Finally, the ZnO/MG hydrogel with a top layer of ZnO nanoparticles was freeze-dried at −80 °C to obtain an ultralight and freestanding ZnO/MG aerogel (Figure 1a, Step 3).

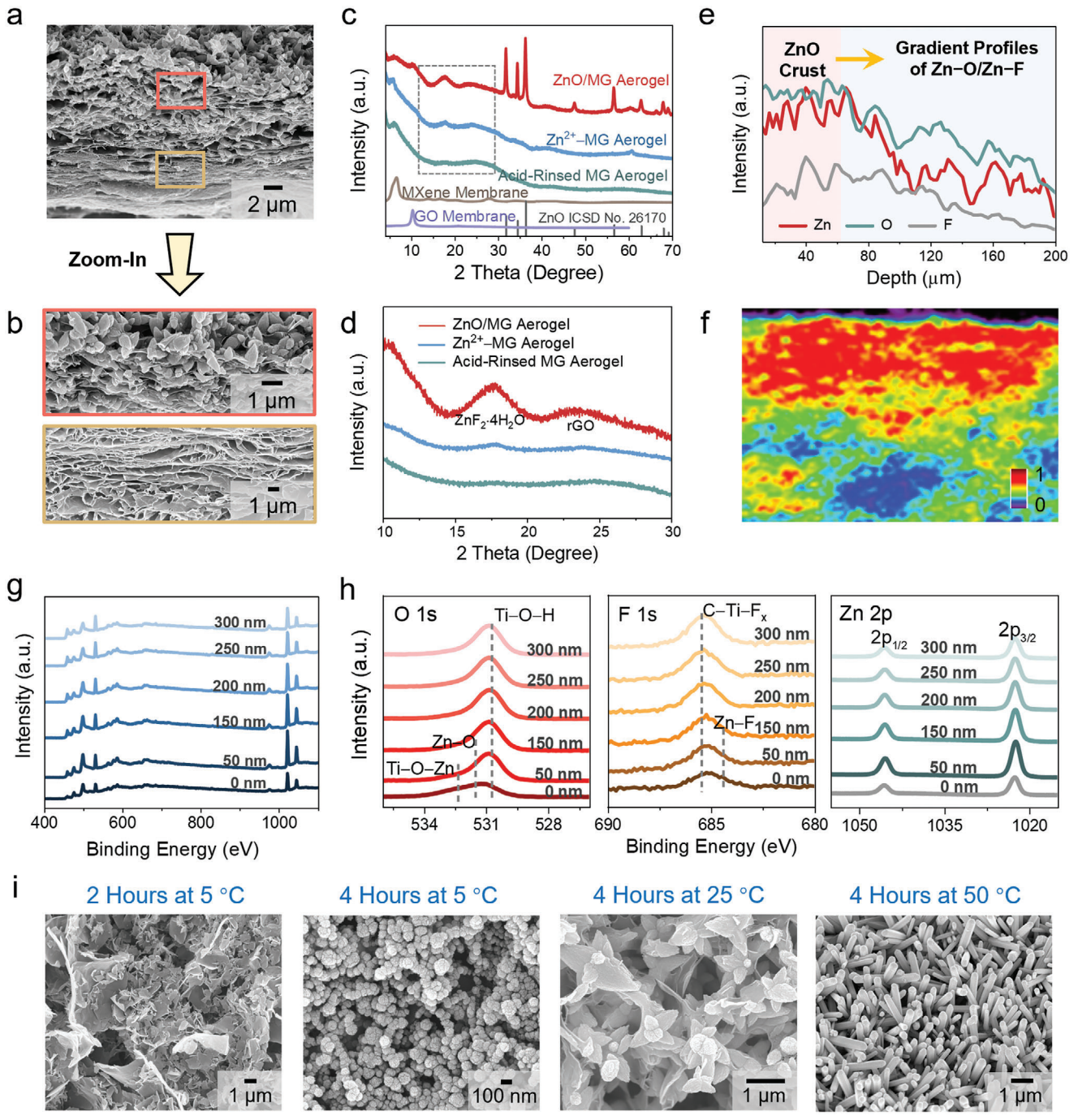

Figure 2. Gradient distributions of Zn–O/Zn–F bonds across ZnO/MG aerogels. a,b) Cross-section SEM images of a ZnO/MG aerogel. c,d) XRD patterns of a ZnO/MG aerogel, a Zn^{2+}–MG aerogel, and an acid-rinsed MG aerogel. e) ToF SIMS depth profiling of Zn and O elements and f) cross-section mapping of Zn element signals across a ZnO/MG aerogel. g,h) XPS depth profiling of a 2-μm-thick ZnO/MG aerogel. i) Top-view SEM images of various ZnO crystals synthesized from different reaction temperatures and time lengths.

2.2. Gradient Distributions of Zn–O/Zn–F Bonds Across ZnO/MG Aerogels

After the freeze-drying step, the compositions and morphologies of ZnO/MG aerogels were characterized via various techniques. Also, two MG aerogels were prepared as control experiments, including Zn^{2+}–MG aerogels (fabricated by directly freeze-drying Zn^{2+}–MG hydrogels without undergoing hydrolysis) and acid-rinsed MG aerogels (fabricated by rinsing Zn^{2+}–MG hydrogels with dilute acid (i.e., HCl) followed by similar hydrolysis and freeze drying processes) (see Figure S8, Supporting Information, for experimental details).

Figure 2a,b shows the cross-section scanning electron microscopy (SEM) images of a ZnO/MG aerogel. At the top-layer surface, a dense crust layer of ZnO nanoparticles was observed, while the bottom part consisted of oriented and aligned pores with size distribution ranging from 1 to 4 μm. As shown in Figure 2c, the XRD pattern of ZnO/MG aerogel exhibits well-indexed peaks of (100), (002), and (101), corresponding to the hexagonal structure of zincite (ZnO, ICSD number: 26 170).[47,53] Also, Figure S9 (Supporting Information) shows the Raman spectrum of a ZnO/MG aerogel, and the active phonon modes at 94.1, 319.8, and 426.8 cm^{-1} correspond to E_2^{low}, $E_2^{high}-E_2^{low}$, and E_2^{high} of ZnO, respectively.[52,54] Interestingly, as shown in Figure 2d, the XRD pattern of ZnO/MG aerogel presents an obvious peak at 17.5°, which coheres to the representative peak of amorphous $ZnF_2{\bullet}4H_2O$ (ICSD number: 10 211). As further demonstrated in Figure S10a (Supporting Information), the XPS spectrum of ZnO/MG aerogel shows the Zn−F peak at 684.5 eV.[34]

As shown in Figure 2e, the depth distributions of Zn and O elements across a ZnO/MG aerogel were investigated via time-of-flight secondary ion mass spectroscopy (ToF SIMS). As the etching depth increased, the intensities of Zn, O, and F element signals continued to decrease, revealing that the ZnO crust layer was able to penetrate the MG aerogel to one-third of the total thickness, while the gradient layer (consisting of the ZnO crust and gradient Zn−O/Zn−F bonds) penetrated up to 50% of the total thickness. The investigation results of penetration depths were consistent with the cross-sectional Zn mapping, as shown in Figure 2f. Furthermore, XPS was conducted on the top and bottom layers of a ZnO/MG aerogel, the Zn−F peak was only found at the top-layer surface, while no Zn−F peak was detected at the bottom-layer surface (Figure S10a, Supporting Information). Also, the Zn−O peak at the top layer showed a higher signal intensity than the one at the bottom layer (Figure S10b,c, Supporting Information). By conducting the XPS depth profiling on a thinner ZnO/MG aerogel (≈2-μm-thick) (Figure 2g,h), the intensities of Zn−O peaks and Zn signals continued to decrease as the etching depth increased from 50 to 300 nm. Similarly, the intensities of Zn−F peaks decreased as the etching depth increased. These ToF SIMS and XPS results verified that Zn−O and Zn−F bonds were distributed with gradients across the ZnO/MG aerogels.

As shown in Figure 2d, the XRD pattern of ZnO/MG aerogel presents a broad plateau at ≈23°, indicating that GO nanosheets were partially reduced into reduced GO (rGO) that benefited the electrical conductivity of ZnO/MG aerogels. The Raman spectrum of ZnO/MG aerogel in Figure S9 (Supporting Information) shows an increased I_D/I_G ratio, and the XPS spectrum in Figure S11 (Supporting Information) exhibits an increased C−C peak intensity, both of which prove the existence of rGO. Also, Raman spectra and thermogravimetric analysis (TGA) were further conducted to quantify the rGO weight ratio (ω_{rGO}) by fabricating a Zn^{2+}−rGO aerogel. As shown in Figure S12a (Supporting Information), the I_D/I_G ratio of the Zn^{2+}−rGO aerogel was 1.29, higher than the I_D/I_G ratio of GO powders (0.97), indicating that GO nanosheets underwent partial reduction by accepting electrons from Zn metal during the voltage-driven Zn^{2+} release process. The ω_{rGO} of a Zn^{2+}−rGO aerogel was calculated to be 49.6% (Figure S12b, Supporting Information, see detailed calculation in Note S1, Supporting Information). In comparison, either ZnO nanocrystals or amorphous $ZnF_2{\bullet}4H_2O$ signals were detected in two control aerogels (i.e., Zn^{2+}−MG and acid-rinsed MG aerogels). From the above chemical characterizations, two indispensable conditions are necessary to synthesize ZnO nanoparticles and achieve gradient Zn−F distributions: i) $Zn(OH)_2$-saturated surfaces and ii) neutral aqueous environment.

As the diffusion rates of Zn^{2+} and OH^- played key roles in the $Zn(OH)_2$ hydrolysis reaction, the sizes and morphologies of ZnO nanoparticles were controlled by adjusting the reaction temperature and time length.[42,55–57] Different ZnO morphologies were obtained in the ZnO/MG aerogels, including ZnO nanoplates (2-h hydrolysis at 5 °C, Figure 2i; Figure S13, Supporting Information), ZnO nanospheres (4-h hydrolysis at 5 °C, Figure 2i; Figure S14, Supporting Information), ZnO nanoflowers (4-h hydrolysis at 25 °C, Figure 2i; Figure S15, Supporting Information), and ZnO nanorods (4-h hydrolysis at 50 °C, Figure 2i; Figure S16, Supporting Information). Figure S17 (Supporting Information) shows the corresponding XRD patterns. Meanwhile, energy dispersive spectroscopy (EDS) was performed to analyze the penetration depths of ZnO crust layers in the ZnO/MG aerogels synthesized from different hydrolysis conditions. As shown in the depth profiling in Figure S18 (Supporting Information), the ZnO/MG aerogel (from 4-h hydrolysis at 25 °C) exhibited the deepest penetration depth, reaching up to 50% of the total thickness. On the other hand, the ZnO/MG aerogel (from 4-h hydrolysis at 50 °C) showed a much shallower penetration depth, accounting for only 6% of the total thickness. The elevated temperature accelerated the hydrolytic reaction kinetics at the water–hydrogel interface, leading to a faster depletion of trapped Zn^{2+} ions within the Zn^{2+}−MG hydrogel. For the ZnO/MG aerogel (from 2-h hydrolysis at 5 °C), there was a minor gradient in the concentration of Zn^{2+}, which was attributed to the slower rates of both ZnO nucleation and Zn^{2+} diffusion at lower temperatures, and these findings aligned with the corresponding cross-section SEM images provided in Figure S19 (Supporting Information). Therefore, the penetration depths of ZnO crust layers and gradient Zn−O/Zn−F distributions can be modulated by controlling the hydrolysis temperatures and time lengths, given that the nucleation and growth rates of ZnO dominated the distribution patterns of Zn elements. For the following electrochemical studies, the ZnO/MG aerogels from 4-h hydrolysis at 25 °C were adopted for the following studies, because of high ZnO crystallinity and neglectable MXene oxidation.

2.3. Effective HER Suppression and Fast Electrochemical Kinetics of ZnO/MG Aerogel Electrodes

As shown in **Figure 3**a and Figure S20 (Supporting Information), a thin ZnO/MG aerogel (2.0-μm-thick) on a Zn plate was fabricated (abbreviated as ZnO/MG aerogel–Zn), which was applied as an electrode for Zn metal deposition. As control experiments, two electrodes were also prepared, including 1) a bare Zn electrode and 2) a non-gradient electrode. The non-gradient electrode was fabricated by directly coating the mixture of ZnO nanoparticles and MG nanosheets on a Zn plate followed by freeze-drying.

As illustrated in Figure 3b, the ZnO/MG aerogel–Zn electrode exhibited a dense crust layer of ZnO nanoparticles and gradient

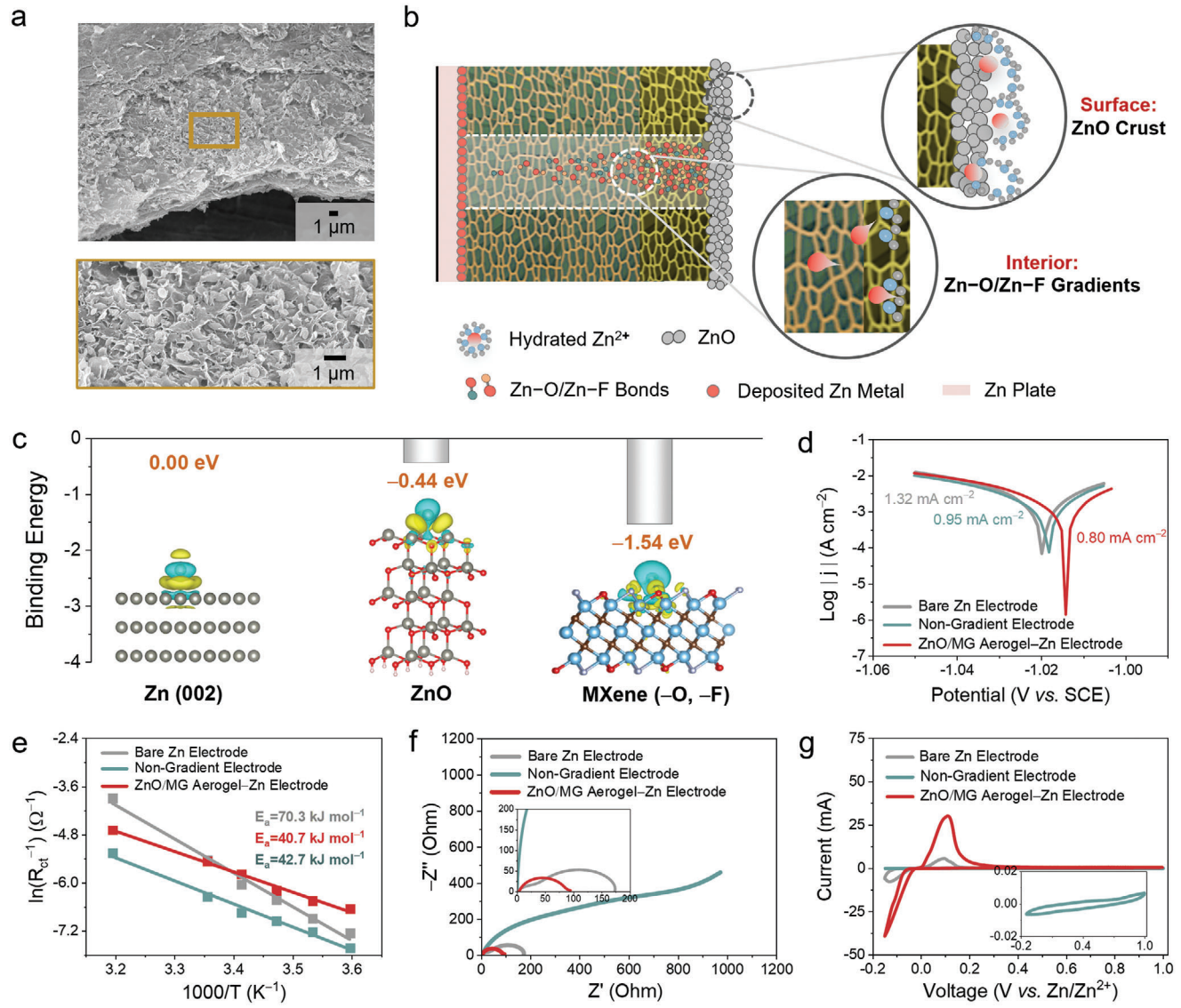

Figure 3. Effective HER suppression and fast electrochemical kinetics of ZnO/MG aerogel electrodes. a) Side-view SEM images of a ZnO/MG aerogel–Zn electrode. b) Schematic illustration of Zn metal deposition processes in a ZnO/MG aerogel–Zn electrode. c) DFT calculations of the binding energies of Zn atoms onto different surfaces of ZnO/MG aerogels. The inset shows the corresponding models with different degrees of electron polarizations at the interfaces. d) Tafel polarization curves of various electrodes at the scan rate of 1.0 mV s^{-1} (in a three-electrode system). e) Fitted Arrhenius plots of the symmetric cells with various electrodes. f) Nyquist plots of symmetric cells with various electrodes. g) CV curves of the asymmetric cells with various counter electrodes at the scan rate of 1.0 mV s^{-1}.

Zn–O/Zn–F distributions, allowing effective HER suppression and fast electrochemical kinetics during Zn metal deposition. To verify the HER suppression effects, multiple density functional theory (DFT) calculations were performed to investigate the binding energies and interfacial charge densities of Zn atoms on different surfaces of the ZnO/MG aerogels.[14,58,59] In Figure 3c, the binding energies of Zn atoms on ZnO nanoparticles and MXene substrate (with terminated –O, –F groups) were calculated to be –0.44 and –1.54 eV, respectively, indicating the zincophilicity nature of ZnO/MG aerogels. As shown in the inset of Figure 3c, the Zn||ZnO and Zn||MXene models exhibited large electron polarizations at the interfaces, confirming the strong affinity between Zn atoms and ZnO/MG aerogels. In contrast, the binding energy of Zn atoms on the Zn metal (002) substrate was low at 0.00 eV, showing poor adsorption mechanism. Furthermore, the zincophilic nature of ZnO/MG aerogels was proved by the ultralow electrolyte (2.0 M $ZnSO_4$) contact angle (θ) of 0° in Figure S21 (Supporting Information), compared with a Zn plate ($\theta \approx$ 83°). Benefiting from the zincophilic nature and strong affinity between Zn and ZnO nanoparticles (and MXene), first, the electronically insulative ZnO crust layer was able to strip the water sheath of hydrated Zn^{2+}. Second, the interior MXene with terminated –O and –F groups were effective to attract Zn^{2+} to the aerogel surfaces, so HER was largely suppressed during Zn metal deposition. Still, the interior electrically conductive MXene (with terminated –O, –F groups) with strong Zn^{2+} affinity facilitated

homogeneous electron/Zn^{2+} fluxes to avoid the growth of Zn dendrites during Zn deposition.

To measure the resistance against HER corrosion, a three-electrode system with a ZnO/MG aerogel–Zn working electrode, a Pt foil counter electrode, and a saturated calomel reference electrode (SCE) was configured. By recording the Tafel polarization curve, the corrosion current density (j_0), as well as the corrosion potential (η), were derived. As shown in Figure 3d, the ZnO/MG aerogel–Zn electrode demonstrates a more positive η of −1.014 V and a smaller j_0 of 0.80 mA cm^{-2} than the non-gradient electrode (η = −1.018 V, j_0 = 0.95 mA cm^{-2}) and the bare Zn electrode (η = −1.020 V, j_0 = 1.32 mA cm^{-2}). Meanwhile, as shown in the linear sweep voltammetry (LSV) plots (Figure S22, Supporting Information), the HER activities of three electrodes were tested. Compared with the two controls, the ZnO/MG aerogel–Zn electrode exhibited suppressed HER activities with a lower catalytic current and a larger onset potential, demonstrating a higher hydrogen evolution resistance.

To further validate the suppressed HER activities, three symmetric cells were fabricated using pairs of ZnO/MG aerogel–Zn, bare Zn, and non-gradient electrodes, named ZnO/MG aerogel–Zn, bare Zn, and non-gradient cells. Afterward, the activation energy (E_a) of Zn deposition (mainly constrained by the energy barrier of Zn^{2+} desolvation) in each cell was evaluated by conducting electrochemical impedance spectroscopy (EIS) measurements at different temperatures (Figure S23, Supporting Information).[53,60,61] As presented in the Arrhenius plot in Figure 3e, the E_a of each cell was quantitively characterized. The E_a of the ZnO/MG aerogel–Zn cell (40.7 kJ mol^{-1}) was smaller than the E_a of the non-gradient (42.7 kJ mol^{-1}) and bare Zn cells (70.3 kJ mol^{-1}), showing that the dense ZnO layer and gradient Zn−O/Zn−F bonds collectively removed water molecules and attenuated the desolvation barrier of hydrated Zn^{2+}.[16,53]

Next, to investigate the electrochemical kinetics, the charge transfer resistance (R_{ct}) of each symmetric cell was characterized via EIS. As shown in Figure 3f, the ZnO/MG aerogel–Zn cell demonstrates a much lower R_{ct} (<86 Ω) than the bare Zn (>173 Ω) and non-gradient cells (>800 Ω). Furthermore, the chronoamperometry (CA) method was adopted to investigate the polarization currents under a constant voltage of 10 mV (vs Zn/Zn^{2+}). As shown in Figure S24 (Supporting Information), the ZnO/MG aerogel–Zn cell demonstrates a high and steady anodic current, especially at the first 500 s, showing a fast rate of releasing Zn^{2+}. In contrast, the bare Zn and non-gradient cells exhibited smaller and fluctuating anodic currents.

Furthermore, the asymmetric cell was fabricated using a ZnO/MG aerogel (≈250-µm-thick) as the working electrode, a Zn plate as the counter electrode, and a 2.0 M $ZnSO_4$ solution as the electrolyte. Meanwhile, two control cells were fabricated by using a Ti foil and a non-gradient electrode (coated on Ti foil) as the working electrodes. As shown in the cyclic voltammetry (CV) curves (Figure 3g), the ZnO/MG aerogel–Zn cell demonstrates the largest integrated area and the lowest onset potentials for Zn plating/stripping (at −0.04/+0.01 V), showing optimal dynamics of electron/Zn^{2+} transport. In comparison, the non-gradient cell did not output any Zn plating/stripping signals due to large internal resistances.

2.4. Asymmetric- and Symmetric-Cell Performance of ZnO/MG Aerogel Electrodes

The advantageous electrochemical properties of ZnO/MG aerogel electrodes were validated in both asymmetric and symmetric cells. As shown in **Figure 4**a, the asymmetric cell with a ZnO/MG aerogel electrode exhibits a low nucleation overpotential of 21.5 mV, indicating an ultralow energy barrier for Zn deposition. The Zn metal deposition was facilitated by the zincophilic surfaces of ZnO/MG aerogel covered with Zn−O/Zn−F bonds. In contrast, the cell with a Ti foil electrode showed a much higher nucleation overpotential of 50.3 mV, and the cell with a non-gradient electrode suffered from voltage fluctuations and ultrahigh nucleation overpotential >300 mV due to large internal resistances.

To evaluate the reversibility of Zn plating/stripping, Figure 4b presents the Coulombic efficiencies of three asymmetric cells with different working electrodes at a large current density of 80 mA cm^{-2}. The cell with a ZnO/MG aerogel electrode demonstrated an average Coulombic efficiency of 99.2% and superior stability over 1600 cycles. As shown in Figure 4c, the cell with a ZnO/MG aerogel electrode presents a low and stable voltage hysteresis of 180 mV even after 1400 cycles. On the other hand, the cell with a Ti foil electrode was out of service after 200 cycles, due to severe HER corrosion and dendrite formation. Similarly, the cell with a non-gradient electrode showed drastic Coulombic efficiency decreases (to 30% after 60 cycles), suffering from large internal resistances and retarded ionic mobility during Zn plating/stripping.

Next, a symmetric cell with two ZnO/MG aerogel–Zn electrodes was fabricated and compared with various control symmetric cells. First, two control cells with bare Zn and non-gradient electrodes were assembled for comparison. Figure 4d,e demonstrates that the ZnO/MG aerogel–Zn cell exhibited a stable voltage profile up to 1200 h at the current densities of 5 and 10 mA cm^{-2}, respectively. Also, the ZnO/MG aerogel–Zn cell showed an ultralow overpotential of <55 mV both at 5 and 10 mA cm^{-2} during cycling. On the other hand, the symmetric cell with two bare Zn electrodes showed continual increases in voltage polarization (>200 mV, at 5 mA cm^{-2}) and voltage fluctuations (>400 mV, at 10 mA cm^{-2}), and it was eventually out of service within 200 h. The symmetric cell using two non-gradient electrodes failed after a few cycles, which was mainly due to large internal resistances. Second, as shown in Figures S25 and S26 (Supporting Information), four more control symmetric cells were fabricated for further comparison, including the cells with ZnO coated−Zn, MXene coated−Zn, GO coated−Zn, and ZnO/rGO aerogel−Zn electrodes. Among the four cells, the ZnO/MG aerogel−Zn electrode demonstrated the longest lifespan with the smallest overpotential. However, the MXene coated−Zn electrode showed unstable current responses after only 50 cycles, due to serious dendrite formation on its top conductive surface. While the symmetric cells using GO coated−Zn and ZnO coated−Zn electrodes had small overpotentials at the first dozen cycles, they eventually failed within 80 cycles due to severe HER corrosion and unstable interfaces between GO (or ZnO) layer and Zn plates. The cell with ZnO/rGO aerogel–Zn electrodes exhibited smaller Zn nucleation overpotentials (≈0.08 V) compared to the cell with bare

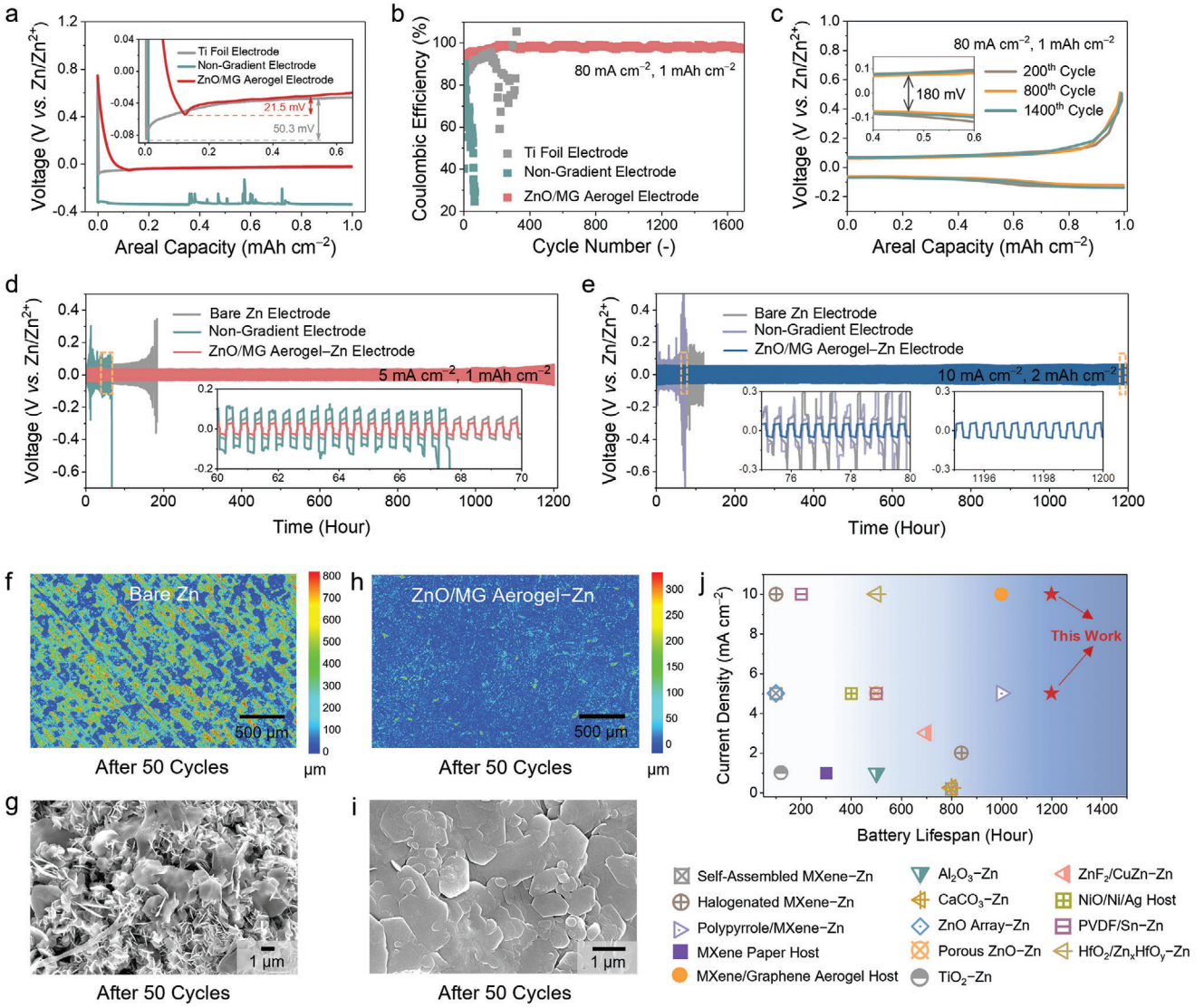

Figure 4. Asymmetric- and symmetric-cell performance of ZnO/MG aerogel electrodes. a,b) Zn nucleation overpotentials and Coulombic efficiencies of the asymmetric cells using various working electrodes. c) Voltage profiles of the asymmetric cell using a ZnO/MG aerogel working electrode during long-term cell operation. Galvanostatic voltage profiles of various symmetric cells at the current densities of d) 5 and e) 10 mA cm^{-2}. Insets are the enlarged voltage profiles at specific time intervals. f,g) CLSM and SEM images of bare Zn electrode after 50 cycles of Zn plating/stripping. h,i) CLSM and SEM images of ZnO/MG aerogel–Zn electrode after 50 cycles of Zn plating/stripping. j) Comparison of symmetric-cell performance of ZnO/MG aerogel–Zn electrodes with reported MXene-decorated Zn electrodes, MXene-based Zn metal hosts, metal oxide-based Zn electrodes, and other gradient electrodes.

Zn electrode (≈0.11 V) during the initial cycles. However, the cell with ZnO/MG aerogel–Zn electrodes showed the lowest overpotentials of 0.05 V. The higher overpotential in the cell with ZnO/rGO aerogel–Zn electrodes was primarily due to the insufficient electrical conductivities of the electrodes. Additionally, this unsatisfactory electrical conductivity led to an uneven distribution of electrons, resulting in deteriorated dendrite formation during battery cycling and eventually causing an internal short circuit at the 200th cycle. Third, the electrochemical performance of ZnO/MG aerogel–Zn electrodes with different gradient thicknesses (synthesized from different hydrolysis conditions) was investigated in symmetric cells. As shown in the inset of Figure S27 (Supporting Information), the cells with three different aerogel electrodes exhibited similar voltage profiles with small overpotentials at the first few cycles. However, the cell with ZnO/MG aerogel–Zn electrodes synthesized at 5 °C failed first after 30 cycles, due to dendrite formation and ineffective HER suppression. Similarly, the cell using ZnO/MG aerogel–Zn electrodes synthesized at 50 °C experienced drastic voltage fluctuations after 40 cycles. This was attributed to poor electrode conductivity, as MXene nanosheets and Zn metal plates were oxidized during the hydrolysis process in a high-temperature water bath. It is worth noting that, during the hydrolysis reaction at 50 °C, the Zn metal plate was immersed in a high-temperature water bath, resulting in the Zn metal oxidation.

The cyclic stability of ZnO/MG aerogel−Zn electrodes was evaluated through multiple characterization techniques. First, Ex situ confocal laser scanning microscopy (CLSM) and SEM were employed to investigate the morphological evolution of a ZnO/MG aerogel−Zn electrode during the cycling test. Before cell operation, the ZnO/MG aerogel−Zn electrode had a uniform crust layer composed of ZnO nanoparticles (Figure S28a,b, Supporting Information). After 50 cycles, the ZnO/MG aerogel−Zn electrode maintained a flat and smooth surface (Figure 4h; Figure S29a,b, Supporting Information, at the stripped state). Also, hexagonal Zn metal platelet deposits were observed, as shown in Figure 4i and Figure S30a (Supporting Information) and the ZnO/MG aerogel layer remained intact and firmly adhered to the Zn plate after the 50th cycle of Zn plating (cross-section SEM images in Figure S31a, Supporting Information, at the plated state), suggesting that the ZnO/MG aerogel-Zn electrode effectively prevented HER corrosion and suppressed dendrite formation. On the other hand, the bare Zn electrode led to serious growth of Zn dendrites with corroded pits, holes (Figure 4f,g; Figure S30b, Supporting Information), and irregular interstices (Figure S31b, Supporting Information), attributed to significant dendrite growth and HER corrosion caused by electrolyte permeation. Second, the crystallinity of a ZnO/MG aerogel–Zn electrode and a bare Zn electrode after cycling tests were analyzed using XRD. As shown in Figure S32 (Supporting Information), the bare Zn electrode (after cycling) exhibited a prominent peak at ≈7.9°, which was identified as $Zn_4SO_4(OH)_6{\cdot}5H_2O$, a known HER byproduct,[10,62,63] confirming the occurrence of significant HER corrosion. In contrast, the ZnO/MG aerogel–Zn electrode did not exhibit a peak at 7.9° after cycling, indicating effective suppression of HER corrosion. Moreover, the ZnO/MG aerogel–Zn electrode displayed a stronger Zn metal (002) peak at 36° after cycling, suggesting the deposition of Zn in a planar-like morphology.[10,58,64] Third, EDS depth profiling was adopted to examine the cyclic stability of the gradient Zn−O profile in ZnO/MG aerogel–Zn electrode after completing 50 cycles of Zn plating/stripping. Figure S33 (Supporting Information) shows that the cycled ZnO/MG aerogel–Zn electrode, in its stripped state, retained similar gradient distributions of Zn and O elements as the initial electrode before cycling (Figure 2e).

Figure 4j further compares the symmetric-cell performance of ZnO/MG aerogel−Zn electrodes with the state-of-the-art electrodes (MXene-decorated Zn electrodes/MXene-based Zn metal hosts, metal oxide-based Zn electrodes, and other gradient electrodes, see detailed comparison in Table S1, Supporting Information).[19–21,33–36,53,65–70] Compared with other MXene-decorated Zn metal electrodes in the literature, the ZnO/MG aerogel−Zn electrode demonstrated long-term cycling stability of >1200 h, higher than self-assembled MXene−Zn electrode (100 h),[65] halogenated MXene−Zn electrode (100 h),[66] and polypyrrole/MXene−Zn electrode (1000 h).[67] Compared with the MXene-based Zn metal hosts, the ZnO/MG aerogel−Zn electrode exhibited effective HER suppression capability and did not require any Zn metal pre-plating step, and the electrode still demonstrated higher cycling stability (>1200 h) than MXene paper host (300 h)[69] and MXene/graphene aerogel host (1000 h),[70] making it more suitable for practical applications of Zn metal anodes. Compared with other metal oxide-based Zn metal electrodes in the literature, the ZnO/MG aerogel−Zn electrode demonstrated the highest current density of 10 mA cm^{-2}, which is higher than TiO_2−Zn electrode (1 mA cm^{-2}),[19] $CaCO_3$−Zn electrode (0.25 mA cm^{-2}),[20] Al_2O_3−Zn electrode (1 mA cm^{-2}),[21] ZnO array−Zn electrode (5 mA cm^{-2}),[68] and porous ZnO−Zn electrode (5 mA cm^{-2}).[53] Moreover, the ZnO/MG aerogel−Zn electrode (10 mA cm^{-2} and >1200 h) outperformed other gradient electrodes both in current densities and cycling stability, including ZnF_2/CuZn−Zn (3 mA cm^{-2} and >700 h),[34] NiO/Ni/Ag host (5 mA cm^{-2} and >400 h),[33] PVDF/Sn−Zn (5 mA cm^{-2} and >500 h),[35] and HfO_2/Zn_xHfO_y−Zn electrodes (10 mA cm^{-2} and >500 h).[36] The high rates and superior stability of ZnO/MG aerogel−Zn electrode mainly benefited from its gradient structures, compositions, and electrical conductivities, enabling synergistic impacts on suppressing HER activities without sacrificing the electrochemical kinetics of Zn stripping/plating.

2.5. Full-Cell Performance of ZnO/MG Aerogel−Zn Anodes

For practical exploitations, a full cell was fabricated using a ZnO/MG aerogel−Zn electrode as the anode, a MnO_2 electrode as the cathode, and 2.0 M $ZnSO_4$ and 0.1 M $MnSO_4$ solution as the aqueous electrolyte. Meanwhile, a control cell using a bare Zn anode was fabricated. As shown in **Figure 5**a and Figure S34 (Supporting Information), the full cell with a ZnO/MG aerogel−Zn anode shows the CV curve with a large integrated area, showing more efficient redox processes with minimized side reactions. Also, the full cell with a ZnO/MG aerogel−Zn anode demonstrated small overpotentials with two pairs of reduction/oxidation peaks at 1.39/1.57 and 1.24/1.61 V (Figure 5a).[53,71] These results demonstrate that the gradient distribution of Zn−O/Zn−F bonds not only suppressed unfavorable HER reactions but also preserved sufficient active sites on MXene/rGO nanosheets to promote full-cell electrochemical reactions with small voltage polarization.

Figure 5b shows the charge–discharge profiles of the full cell with a ZnO/MG aerogel−Zn anode at various current densities, and Figure S35 (Supporting Information) displays the profiles for the first three activation cycles. Compared with the control cell with a bare Zn anode (Figure 5c), the ZnO/MG aerogel−Zn anode showed high full-cell capacities with small voltage hysteresis across a wide range of current densities (0.2–2.0 A g^{-1}). As further demonstrated in Figure 5d, the full cell with a ZnO/MG aerogel−Zn anode exhibited higher rate performance (from 0.2 to 2.0 A g^{-1}) and better capacity recoverability than the control cell. The cycling performance of the full cells with ZnO/MG aerogel−Zn and bare Zn anode was further evaluated, as shown in Figure 5e. Both full cells showed similar capacities at the initial five activation cycles (at 0.2 A g^{-1}). However, a significant capacity drop was observed in the full cell with bare Zn anode when the current density increased to 1.0 A g^{-1}, primarily due to the large charge transfer resistances and poor electrochemical kinetics at high current densities. It should be noted that the capacity increase trends during the first 50 cycles are attributed to the gradual activation process of the cathode's active materials (i.e., MnO_2) under a high current density of 1.0 A g^{-1}.[72,73] Meanwhile, the full cell maintained a high specific capacity of 148.6 mAh g^{-1} after 500 cycles (Figure 5e), showing higher

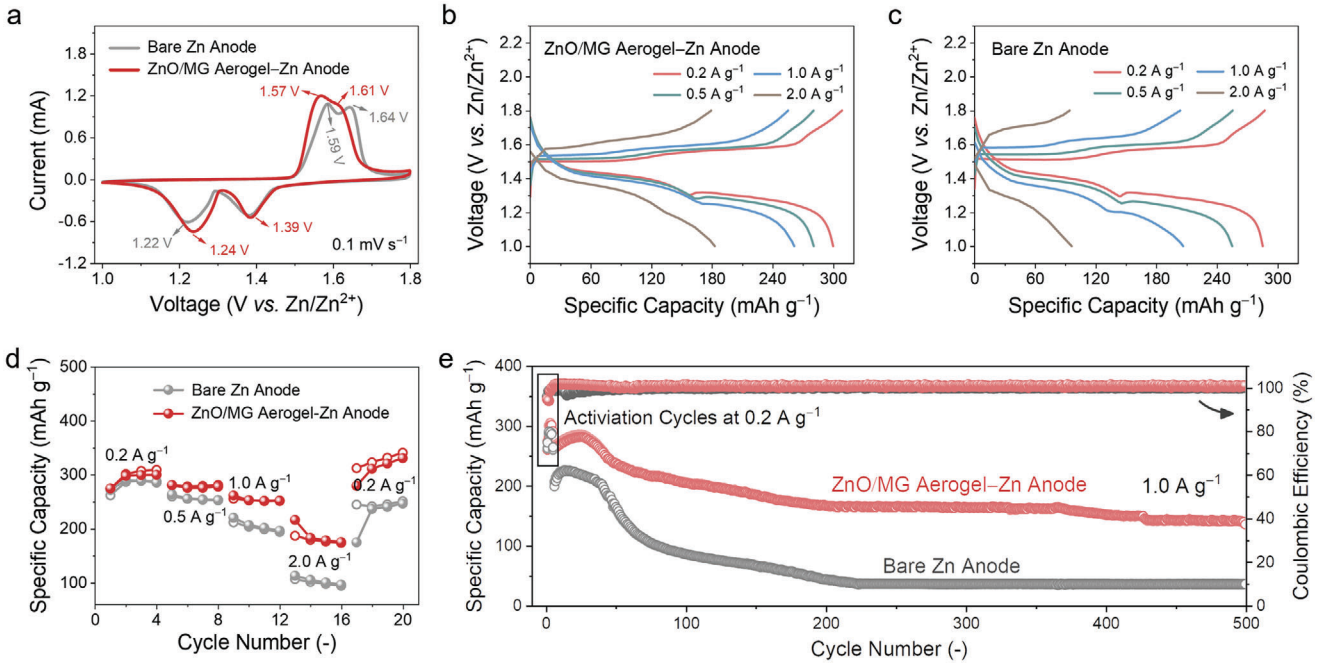

Figure 5. Full-cell performance of ZnO/MG aerogel–Zn anodes. a) CV curves of the full cells with ZnO/MG aerogel–Zn and bare Zn anodes at a scan rate of 0.1 mV s^{-1}. Charge–discharge profiles of the full cells with b) ZnO/MG aerogel–Zn and c) bare Zn anodes at various current densities. d) Rate performance (solid circles: discharge capacities, empty circles: charge capacities) and e) cycling tests of the full cells with ZnO/MG aerogel–Zn and bare Zn anodes. The voltage window of full cells was 1.0–1.8 V (vs Zn/Zn^{2+}).

capacity retention of 60.6% with stable Coulombic efficiency (≈100%). On the other hand, the control cell with a bare Zn anode exhibited poor rate performance, the full-cell capacity decayed quickly to 33.2 mAh g^{-1} after 200 cycles, showing low capacity retention of 15.6%. These results confirm that the ZnO/MG aerogels with ZnO crust interfaces and gradient Zn–O/Zn–F bonds can promote high-rate battery performance and maintain long battery service time with a high-capacity retention, fulfilling the requirements of high-rate and long-term electrochemical performance, and long-duration energy storage capabilities on ZIBs.

3. Conclusion

In summary, the ZnO/MG aerogel–Zn electrodes with gradient structures, compositions, and electrical conductivities were produced through a Zn^{2+}-induced assembly strategy and the ZnO/MG aerogel–Zn electrodes served as highly stable Zn metal anodes. Without the use of reagents, solvents, or thermal treatments, the ZnO/MG aerogel–Zn electrode was fabricated in an environmentally friendly manner. Also, the morphology of the ZnO crust layer was controllable by simply altering the time/temperature of a hydrolysis reaction. Our electrochemical studies revealed that the ZnO crust layer and the gradient Zn–O/Zn–F profiles collectively suppressed corrosive HER activities and enabled fast desolvation processes of hydrated Zn^{2+} during Zn deposition. Moreover, the abundant oxygen- and fluorine-containing surface groups of the structured MG framework provided zincophilic nature, which was advantageous to guide the homogeneous deposition of hexagonal Zn platelets. Owing to these synergistic effects, the symmetric cells using two ZnO/MG aerogel–Zn electrodes showed small voltage hysteresis as well as superior cycling performance over 1200 h, even at large current densities of 10 mA cm^{-2}. Additionally, the full cell using a ZnO/MG aerogel–Zn anode and a MnO_2 cathode achieved a long battery lifespan at high rates (>500 cycles at 1.0 A g^{-1}) with a capacity retention over 60.6%. This work shows a synergistic strategy to fabricate stable and high-rate Zn metal anodes via gradient structural and compositional design, enabling scalable production and future commercialization of stable Zn metal anodes.

4. Experimental Section

$Ti_3C_2T_x$ MXene and Graphene Oxide (GO) Nanosheets: $Ti_3C_2T_x$ MXene nanosheets dispersion was prepared by adding 1.0 g of Ti_3AlC_2 MAX powder (Laizhou Kai Kai Ceramic Materials Co., Ltd, China) into the solution containing 1.0 g of lithium fluoride (LiF, 99%, Sigma–Aldrich) and 20 mL of 6.0 M hydrochloride (HCl) acid followed by 24-h stirring at 400 r.p.m. at 35 °C. Afterward, the solid residue was washed with DI water until the pH value increased to 7.0. Subsequently, the washed residuals were dispersed in 50 mL of DI water, ultrasonicated for 30 min under N_2 protection in an ice bath, and then centrifuged at 3500 r.p.m. for 30 min. The supernatant was collected as the final $Ti_3C_2T_x$ MXene nanosheet suspension with a concentration of ≈6.0 mg mL^{-1}. Graphene oxide (GO) dispersion (10.0 mg mL^{-1}) was purchased from Xianfeng Nano Co., Ltd, China.

Fabrication of Zn^{2+}–MG Hydrogels, ZnO/MG Aerogels, Zn^{2+}–MG Aerogels, and Acid-Rinsed MG Aerogels: MXene and GO dispersions were mixed at 4.0 mg mL^{-1} and a MXene-to-GO weight ratio of 7:3. The Zn^{2+}-induced MXene/GO assembly was conducted in a two-electrode configuration with a Zn plate as the anode, a platinum plate as the cathode, and the MXene/GO mixture as the electrolyte. Before the Zn^{2+}-induced

MXene/GO assembly, the Zn plate was cleaned via ultrasonication in DI water for 15 min. One side of the Zn plate was covered with Kapton tape, so the gelation process only occurred on one side of the Zn plate. The Zn^{2+}-induced assembly process was initiated by applying a constant voltage of −50 mV on the platinum plate for 30 min. Finally, the Zn^{2+}−MG hydrogel (on the Zn plate) was removed from the electrolyte solution and stabilized in the air for 30 min.

For the fabrication of ZnO/MG aerogels, the stabilized Zn^{2+}−MG hydrogels (on the Zn plates) were immersed into DI water at different temperatures (5, 25, and 50 °C) for several hours (2 or 4 h). Afterward, the Zn^{2+}−MG hydrogels underwent in situ hydrolysis reaction to synthesize ZnO nanocrystals with different geometries. Followed by freeze drying at −80 °C and 5–10 Pa, ZnO/MG aerogels were produced.

For the fabrication of Zn^{2+}–MG aerogels, the Zn^{2+}−MG hydrogels underwent direct freeze drying without conducting in situ hydrolysis reaction. For the fabrication of acid-rinsed MG aerogels, the Zn^{2+}−MG hydrogels were immersed in 0.2 M HCl solution for 5 min, and the Zn^{2+}−MG hydrogels were then detached from the Zn plates. Afterward, the freestanding Zn^{2+}−MG hydrogel was immersed in a DI water bath at room temperature (25 °C) for 4 h. Followed by freeze drying at −80 °C and 5–10 Pa, acid-rinsed MG aerogels were produced.

Fabrication of ZnO/MG Aerogel–Zn Electrodes: For the fabrication of ZnO/MG aerogel–Zn electrodes (on Zn plates), the MXene/GO mixture at a low concentration of 1.0 mg mL^{-1} was adopted, and the time length of Zn^{2+}-induced assembly was controlled to be 120 s. Afterward, similar fabrication steps (air stabilization, in situ hydrolysis reaction from different conditions, and freeze drying) were conducted to produce ZnO/MG aerogel–Zn electrodes. Finally, the ZnO/MG aerogel–Zn electrodes were cut into pieces with the dimension of 1.0 cm × 1.0 cm for further usage.

Fabrication of Zn^{2+}–rGO Hydrogels, Zn^{2+}–rGO Aerogels, ZnO/rGO Aerogel–Zn Electrodes as Control Experiments: With similar fabrication steps, Zn^{2+}–rGO hydrogels were produced by using GO dispersion (4.0 mg mL^{-1}) instead of MXene/GO dispersion, and Zn^{2+}–rGO aerogels were obtained after the freeze-drying process. ZnO/rGO aerogel–Zn electrodes were fabricated with GO dispersion at a low concentration of 1.0 mg mL^{-1}. After conducting air stabilization, in situ hydrolysis reaction (at 25 °C), and freeze drying, ZnO/rGO aerogel–Zn electrodes were produced.

Fabrication of Non-Gradient Electrodes (on Zn Plates or Ti Foils) as Control Experiments: ZnO nanoparticles (99%, Sigma–Aldrich) were mixed in the MXene/GO mixtures (30 wt.% of GO), and the mass ratio of ZnO was controlled to be 70 wt.%. Afterward, the ZnO/MXene/GO slurry was coated on Zn plates or Ti foils followed by freeze drying, and the thicknesses of ZnO/MXene/GO coatings were controlled to be ≈2 µm on Zn plates and ≈250 µm on Ti foils after freeze-drying.

Fabrication of MXene Coated–Zn, GO Coated–Zn, ZnO Coated–Zn Electrodes as Control Experiments: The MXene coated–Zn, GO coated–Zn, ZnO coated–Zn electrodes were prepared by coating MXene, GO, and ZnO slurries on Zn plates, respectively. After freeze-drying, they were cut into pieces with the dimensions of 1.0 cm × 1.0 cm for further usage. All the coating thicknesses were controlled at ≈2.0 µm.

Fabrication of MnO_2 Cathodes: β-MnO_2, Super P carbon black, and poly(vinylidene) fluoride (PVdF) were mixed in *N*-methyl pyrrolidone (NMP) at a weight ratio of 7:2:1, and the slurry was then vigorously stirred overnight. Afterward, the slurry was coated on a Ti foil with an areal loading of ≈2.0 mg cm^{-2} and dried at 80 °C for 12 h. Finally, the MnO_2-coated Ti foil was punched into disks with a diameter of 12 mm for further usage.

Electrochemical Measurements: The HER suppression capability of the ZnO/MG aerogel was studied in a three-electrode system consisting of a ZnO/MG aerogel–Zn working electrode, a Pt plate counter electrode, a saturated calomel reference electrode (SCE), and 50 mL of 2.0 M $ZnSO_4$ electrolyte solution. The Tafel curves were derived from the CV curves with a voltage window from −1.01 to −1.15 V (vs SCE) at a scan rate of 1.0 mV s^{-1}. The hydrogen evolution activity of each electrode was measured by conducting linear sweep voltammetry (LSV) at a scan rate of 1.0 mV s^{-1} (voltage range: open circuit voltage to −1.15 V vs SCE). As control experiments, two three-electrode systems with a non-gradient and a bare Zn working electrode were tested, respectively.

For the electrochemical kinetics analysis, symmetric cells (CR2032 coin cell) using a pair of ZnO/MG aerogel–Zn electrodes, non-gradient electrodes, and bare Zn electrodes were assembled, respectively, and chronoamperometry (CA) tests and electrochemical impedance spectroscopy (EIS) measurements were conducted. The CA test of each symmetric cell was performed under a polarization potential of 10 mV for 4000 s. Charge transfer resistances of symmetric cells were measured by EIS with an amplitude AC signal of 10 mV and a frequency range of 0.1–10^6 Hz under different temperatures. Afterward, an asymmetric cell with a ZnO/MG aerogel–Zn counter electrode, a Ti foil working electrode, and a 2.0 M $ZnSO_4$ electrolyte was assembled. The cyclic voltammetry (CV) measurement was performed in the voltage range of −0.15–1.0 V (vs Zn/Zn^{2+}) at a scan rate of 1.0 mV s^{-1}. Two control experiments, 1) an asymmetric cell composed of a bare Zn counter electrode and a Ti foil working electrode, and 2) an asymmetric cell composed of a non-gradient counter electrode and a Ti foil working electrode, were fabricated.

To investigate the electrochemical performance of ZnO/MG aerogels as Zn metal hosts, an asymmetric cell was assembled with a freestanding ZnO/MG aerogel working electrode, a Zn plate counter electrode, and a 2.0 M $ZnSO_4$ electrolyte. Two control experiments, 1) an asymmetric cell composed of a Ti foil working electrode and a Zn plate counter electrode, and s) an asymmetric cell composed of a non-gradient working electrode (coated on Ti foil) and a Zn plate counter electrode, were prepared. For the Coulombic efficiency tests, the asymmetric cells were discharged at a current density of 80 mA cm^{-2}, and the areal capacity was kept at 1 mAh cm^{-2}, followed by charging to 0.5 V (vs Zn/Zn^{2+}).

To evaluate the cycling stability of ZnO/MG aerogel interfaces anchored on Zn plates, a symmetric cell with a pair of ZnO/MG aerogel–Zn electrodes and 2.0 M $ZnSO_4$ electrolyte was assembled. As control experiments, two symmetric cells composed of a pair of bare Zn and non-gradient electrodes were fabricated. The symmetric cells were charged/discharged at two current densities of 5 mA cm^{-2} (with an areal capacity of 1 mAh cm^{-2}) and 10 mA cm^{-2} (with an areal capacity of 2 mAh cm^{-2}).

All the asymmetric and symmetric cells were assembled with glass fiber separators (Whatman, GF/A) and 2.0 M $ZnSO_4$ electrolyte solution in the air atmosphere. The electrolyte volume was fixed at 100 µL in each cell. They were tested in a Landt battery test system at room temperature. The CA polarization, CV, LSV curves, and EIS plots were recorded by using an electrochemical workstation (Autolab, PGSTAT302N).

For the full cell fabrication, a coin cell composed of a ZnO/MG aerogel–Zn anode, a β-MnO_2 cathode, and 2.0 M $ZnSO_4$ + 0.1 M $MnSO_4$ (100 µL) electrolyte was assembled. They were tested at various current densities with the voltage range of 1.0–1.8 V (vs Zn/Zn^{2+}) at room temperature. As a control experiment, a full cell composed of a bare Zn anode and a β-MnO_2 cathode was fabricated.

Computational Methods: Density functional theory (DFT) analysis was conducted utilizing the Vienna Ab initio Simulation Package (VASP).[74] The Perdew–Burke–Ernzerhof (PBE) functionals within the generalized gradient approximation were utilized for exchange-correlation energy calculations.[75] Energy convergence criteria were set at 10^{-4} eV, and a force convergence threshold of 0.01 eV $Å^{-1}$ was applied. To calculate the binding energy between Zn atoms and Zn metal, a Zn metal (002) plane was used. To calculate the binding energy between Zn atoms and MXene substrate, a $Ti_3C_2T_x$ MXene model with terminated −O, −F groups was constructed. To calculate the binding energy between Zn atoms and ZnO substrate, a ZnO model with a slab arrangement and a Zn-terminated polar surface was configured. To account for periodic boundary conditions, a vacuum slab with a thickness of 20 Å was introduced during the binding energy computation.

The binding energy (E_b) was calculated using the following equation:

$$E_b = E_{total} - (E_{sub} + E_{Zn}) \quad (5)$$

where E_{total} is the total energy of the model, E_{sub} and E_{Zn} are the energies of the substrate and Zn atom after relaxation, respectively.

Materials Characterization: X-ray diffraction (XRD) patterns were recorded by an X-ray diffractometer (Rigaku SmartLab, 9 kW,

Cu K_α radiation, $\lambda = 0.154$ nm) with a scan rate of 2° min^{-1}. Morphologies and elemental mappings were obtained using a field emission scanning electron microscope (FESEM, FEI Nova NanoSEM 450) operating at 10.0 kV, equipped with an energy dispersive spectroscopy (EDS) for elemental analyses. Morphologies of $Ti_3C_2T_x$ MXene and GO nanosheets were characterized by using a high-resolution transmission electron microscope (HRTEM, JEOL 2010F). Time-of-flight secondary ion mass spectroscopy (ToF SIMS, PHI nano TOF II) was used to analyze the composition distribution across the normal direction of the obtained aerogels. X-ray photoelectron spectrum (XPS) was recorded on an X-ray photoelectron spectrometer (Kratos AXIS UltraDLD) via a monochromatic Al X-ray beam (100 µm, 25 W) and equipped with an Ar^+ sputtering gun, with a photoelectron take-off angle of 90°. Raman spectrum was recorded using Raman microscopy (Thermo Scientific, DXR3) with 532 nm laser excitation. 3D depth information of the electrodes was obtained by using confocal laser microscopy (Lasertec, ECCS B320). Thermogravimetric analysis (TGA) was carried out on a Shimadzu TGA-50 Series system, with the heating rate at 5 °C min^{-1}. All of the TGA measurements were carried out under a N_2 flow.

Supporting Information

Supporting Information is available from the Wiley Online Library or from the author.

Acknowledgements

The authors acknowledge the financial support provided by the Start-Up Fund of the University of Maryland, College Park (KFS No.: 2957431 to P.-Y.C.). Fundings for this research were provided by the MOST-AFOSR Taiwan Topological and Nanostructured Materials Grant under Grant No. FA2386-21-1-4065 (KFS No.: 5284212 to P.-Y.C.), Energy Innovation Seed Grant from Maryland Energy Innovation Institute (MEI^2) (KFS No.: 2957597 to P.-Y.C.), and Grant Challenge Grant (Team Project) from the University of Maryland, College Park (KFS No. 2957821 to P.-Y.C.). Y.Z. acknowledges the Key Program of the National Natural Science Foundation of China (No. 51732005). Z.P. acknowledges the support from the National Natural Science Foundation of China (NSFC) (No. 12302143). Y.L. acknowledges the financial support provided by the Maryland Robotics Center (MRC) for a research fellowship.

Conflict of Interest

The authors declare no conflict of interest.

Data Availability Statement

The data that support the findings of this study are available from the corresponding author upon reasonable request.

Keywords

cation-induced assembly, gradient structures and compositions, $Ti_3C_2T_x$ MXene aerogels, zinc-ion batteries, Zn metal anodes

Received: May 23, 2023
Revised: October 7, 2023
Published online: November 12, 2023

[1] Z. Liu, Y. Huang, Y. Huang, Q. Yang, X. Li, Z. Huang, C. Zhi, *Chem. Soc. Rev.* **2020**, *49*, 180.
[2] L. E. Blanc, D. Kundu, L. F. Nazar, *Joule* **2020**, *4*, 771.
[3] G. Fang, J. Zhou, A. Pan, S. Liang, *ACS Energy Lett.* **2018**, *3*, 2480.
[4] D. Chao, W. Zhou, F. Xie, C. Ye, H. Li, M. Jaroniec, S.-Z. Qiao, *Sci. Adv.* **2020**, *6*, eaba4098.
[5] Y. Zong, H. He, Y. Wang, M. Wu, X. Ren, Z. Bai, N. Wang, X. Ning, S. X. Dou, *Adv. Energy Mater.* **2023**, *13*, 2300403.
[6] D. Chao, S.-Z. Qiao, *Joule* **2020**, *4*, 1846.
[7] J. Yi, P. Liang, X. Liu, K. Wu, Y. Liu, Y. Wang, Y. Xia, J. Zhang, *Energy Environ. Sci.* **2018**, *11*, 3075.
[8] X. Zeng, J. Hao, Z. Wang, J. Mao, Z. Guo, *Energy Storage Mater.* **2019**, *20*, 410.
[9] Z. Yi, G. Chen, F. Hou, L. Wang, J. Liang, *Adv. Energy Mater.* **2021**, *11*, 2003065.
[10] J. Cao, D. Zhang, X. Zhang, Z. Zeng, J. Qin, Y. Huang, *Energy Environ. Sci.* **2022**, *15*, 499.
[11] F. Wang, O. Borodin, T. Gao, X. Fan, W. Sun, F. Han, A. Faraone, J. A. Dura, K. Xu, C. Wang, *Nat. Mater.* **2018**, *17*, 543.
[12] Z. Li, A. W. Robertson, *Battery Energy* **2023**, *2*, 20220029.
[13] W. Du, J. Yan, C. Cao, C. C. Li, *Energy Storage Mater.* **2022**, *52*, 329.
[14] H. Yu, Y. Zeng, N. W. Li, D. Luan, L. Yu, X. W. (.D.). Lou, *Sci. Adv.* **2022**, *8*, eabm5766.
[15] L. Ma, M. A. Schroeder, O. Borodin, T. P. Pollard, M. S. Ding, C. Wang, K. Xu, *Nat. Energy* **2020**, *5*, 743.
[16] H. Yang, Z. Chang, Y. Qiao, H. Deng, X. Mu, P. He, H. Zhou, *Angew. Chem., Int. Ed.* **2020**, *59*, 9377.
[17] V. Vijayakumar, M. Ghosh, M. Kurian, A. Torris, S. Dilwale, M. V. Badiger, M. Winter, J. R. Nair, S. Kurungot, *Small* **2020**, *16*, 2002528.
[18] R. Zhao, Y. Yang, G. Liu, R. Zhu, J. Huang, Z. Chen, Z. Gao, X. Chen, L. Qie, *Adv. Funct. Mater.* **2021**, *31*, 2001867.
[19] K. Zhao, C. Wang, Y. Yu, M. Yan, Q. Wei, P. He, Y. Dong, Z. Zhang, X. Wang, L. Mai, *Adv. Mater. Interfaces* **2018**, *5*, 1800848.
[20] L. Kang, M. Cui, F. Jiang, Y. Gao, H. Luo, J. Liu, W. Liang, C. Zhi, *Adv. Energy Mater.* **2018**, *8*, 1801090.
[21] H. He, H. Tong, X. Song, X. Song, J. Liu, *J. Mater. Chem. A* **2020**, *8*, 7836.
[22] H. Wang, Y. Chen, H. Yu, W. Liu, G. Kuang, L. Mei, Z. Wu, W. Wei, X. Ji, B. Qu, L. Chen, *Adv. Funct. Mater.* **2022**, *32*, 2205600.
[23] J. B. Park, C. Choi, J. H. Park, S. Yu, D.-W. Kim, *Adv. Energy Mater.* **2022**, *12*, 2202937.
[24] M. Zhou, C. Fu, L. Qin, Q. Ran, S. Guo, G. Fang, X. Lang, Q. Jiang, S. Liang, *Energy Storage Mater.* **2022**, *52*, 161.
[25] L. Zhou, F. Yang, S. Zeng, X. Gao, X. Liu, X. Cao, P. Yu, X. Lu, *Adv. Funct. Mater.* **2022**, *32*, 2110829.
[26] H. Tian, Z. Li, G. Feng, Z. Yang, D. Fox, M. Wang, H. Zhou, L. Zhai, A. Kushima, Y. Du, Z. Feng, X. Shan, Y. Yang, *Nat. Commun.* **2021**, *12*, 237.
[27] B. Li, K. Yang, J. Ma, P. Shi, L. Chen, C. Chen, X. Hong, X. Cheng, M.-C. Tang, Y.-B. He, F. Kang, *Angew. Chem., Int. Ed.* **2022**, *61*, e202212587.
[28] J. Zheng, Z. Huang, Y. Zeng, W. Liu, B. Wei, Z. Qi, Z. Wang, C. Xia, H. Liang, *Nano Lett.* **2022**, *22*, 1017.
[29] J. Wu, Z. Ju, X. Zhang, A. C. Marschilok, K. J. Takeuchi, H. Wang, E. S. Takeuchi, G. Yu, *Adv. Mater.* **2022**, *34*, 2202780.
[30] Z. Zhang, S. Guan, S. Liu, B. Hu, C. Xue, X. Wu, K. Wen, C.-W. Nan, L. Li, *Adv. Energy Mater.* **2022**, *12*, 2103332.
[31] J. Yun, B.-K. Park, E.-S. Won, S. H. Choi, H. C. Kang, J. H. Kim, M.-S. Park, J.-W. Lee, *ACS Energy Lett.* **2020**, *5*, 3108.
[32] Y. Nan, S. Li, Y. Shi, S. Yang, B. Li, *Small* **2019**, *15*, e1903520.
[33] Y. Gao, Q. Cao, J. Pu, X. Zhao, G. Fu, J. Chen, Y. Wang, C. Guan, *Adv. Mater.* **2023**, *35*, 2207573.
[34] G. Liang, J. Zhu, B. Yan, Q. Li, A. Chen, Z. Chen, X. Wang, B. Xiong, J. Fan, J. Xu, C. Zhi, *Energy Environ. Sci.* **2022**, *15*, 1086.
[35] Q. Cao, Y. Gao, J. Pu, X. Zhao, Y. Wang, J. Chen, C. Guan, *Nat. Commun.* **2023**, *14*, 641.

[36] J.-L. Yang, L. Liu, Z. Yu, P. Chen, J. Li, P. A. Dananjaya, E. K. Koh, W. S. Lew, K. Liu, P. Yang, H. J. Fan, *ACS Energy Lett.* **2023**, *8*, 2042.
[37] B. Yuan, H. Sun, T. Wang, Y. Xu, P. Li, Y. Kong, Q. J. Niu, *Sci. Rep.* **2016**, *6*, 28509.
[38] Z. Lin, J. Liu, W. Peng, Y. Zhu, Y. Zhao, K. Jiang, M. Peng, Y. Tan, *ACS Nano* **2020**, *14*, 2109.
[39] V. Anand, V. C. Srivastava, *J. Alloys Compd.* **2015**, *636*, 288.
[40] I. Grobelsek, B. Rabung, M. Quilitz, M. Veith, *J. Nanopart. Res.* **2011**, *13*, 5103.
[41] N. Uekawa, R. Yamashita, Y. Jun Wu, K. Kakegawa, *Phys. Chem. Chem. Phys.* **2004**, *6*, 442.
[42] C. Debiemme-Chouvy, J. Vedel, *J. Electrochem. Soc.* **1991**, *138*, 2538.
[43] J. Van Embden, S. Gross, K. R. Kittilstved, E. Della Gaspera, *Chem. Rev.* **2023**, *123*, 271.
[44] S. K. Sharma, *J. Chem. Phys* **1973**, *58*, 1626.
[45] J. S. Fordyce, R. L. Baum, *J. Chem. Phys.* **1965**, *43*, 843.
[46] M. Wang, L. Jiang, E. J. Kim, S. H. Hahn, *RSC Adv.* **2015**, *5*, 87496.
[47] R. Al-Gaashani, S. Radiman, A. R. Daud, N. Tabet, Y. Al-Douri, *Ceram. Int.* **2013**, *39*, 2283.
[48] J. Guo, X. Liu, Y. Cheng, Y. Li, G. Xu, P. Cui, *Curr. Nanosci.* **2010**, *6*, 213.
[49] F. Demoisson, R. Piolet, F. Bernard, *Cryst. Growth Des.* **2014**, *14*, 5388.
[50] C. B. Ong, L. Y. Ng, A. W. Mohammad, *Renewable Sustainable Energy Rev.* **2018**, *81*, 536.
[51] R. Wang, H. Zobeiri, Y. Xie, X. Wang, X. Zhang, Y. Yue, *Adv. Sci.* **2020**, *7*, 2000097.
[52] V. Strelchuk, O. Kolomys, S. Rarata, P. Lytvyn, O. Khyzhun, C. O. Chey, O. Nur, M. Willander, *Nanoscale Res. Lett.* **2017**, *12*, 351.
[53] X. Xie, S. Liang, J. Gao, S. Guo, J. Guo, C. Wang, G. Xu, X. Wu, G. Chen, J. Zhou, *Energy Environ. Sci.* **2020**, *13*, 503.
[54] Y. Jing, Q. Lei, G. Hu, J. He, X. Lei, F. Wang, J. Li, Y. Yang, X. Zhang, *Front. Chem.* **2020**, *8*, 723.
[55] B. Liu, H. C. Zeng, *Langmuir* **2004**, *20*, 4196.
[56] N. A. Jose, M. Kovalev, E. Bradford, A. M. Schweidtmann, H. Chun Zeng, A. A. Lapkin, *Chem. Eng. J.* **2021**, *426*, 131345.
[57] M. Søndergaard, E. D. Bøjesen, M. Christensen, B. B. Iversen, *Cryst. Growth Des.* **2011**, *11*, 4027.
[58] S. Li, J. Fu, G. Miao, S. Wang, W. Zhao, Z. Wu, Y. Zhang, X. Yang, *Adv. Mater.* **2021**, *33*, 2008424.
[59] F. Xie, H. Li, X. Wang, X. Zhi, D. Chao, K. Davey, S.-Z. Qiao, *Adv. Energy Mater.* **2021**, *11*, 2003419.
[60] D. Kundu, S. Hosseini Vajargah, L. Wan, B. Adams, D. Prendergast, L. F. Nazar, *Energy Environ. Sci.* **2018**, *11*, 881.
[61] C. Yan, H.-R. Li, X. Chen, X.-Q. Zhang, X.-B. Cheng, R. Xu, J.-Q. Huang, Q. Zhang, *J. Am. Chem. Soc.* **2019**, *141*, 9422.
[62] J. Hao, L. Yuan, C. Ye, D. Chao, K. Davey, Z. Guo, S.-Z. Qiao, *Angew. Chem., Int. Ed.* **2021**, *60*, 7366.
[63] L. Hong, X. Wu, L.-Y. Wang, M. Zhong, P. Zhang, L. Jiang, W. Huang, Y. Wang, K.-X. Wang, J.-S. Chen, *ACS Nano* **2022**, *16*, 6906.
[64] J. Zheng, Q. Zhao, T. Tang, J. Yin, C. D. Quilty, G. D. Renderos, X. Liu, Y. Deng, L. Wang, D. C. Bock, C. Jaye, D. Zhang, E. S. Takeuchi, K. J. Takeuchi, A. C. Marschilok, L. A. Archer, *Science* **2019**, *366*, 645.
[65] N. Zhang, S. Huang, Z. Yuan, J. Zhu, Z. Zhao, Z. Niu, *Angew. Chem., Int. Ed.* **2021**, *60*, 2861.
[66] X. Li, M. Li, K. Luo, Y. Hou, P. Li, Q. Yang, Z. Huang, G. Liang, Z. Chen, S. Du, Q. Huang, C. Zhi, *ACS Nano* **2022**, *16*, 813.
[67] Y. Zhang, Z. Cao, S. Liu, Z. Du, Y. Cui, J. Gu, Y. Shi, B. Li, S. Yang, *Adv. Energy Mater.* **2022**, *12*, 2103979.
[68] J. Y. Kim, G. Liu, G. Y. Shim, H. Kim, J. K. Lee, *Adv. Funct. Mater.* **2020**, *30*, 2004210.
[69] Y. Tian, Y. An, C. Wei, B. Xi, S. Xiong, J. Feng, Y. Qian, *ACS Nano* **2019**, *13*, 11676.
[70] J. Zhou, M. Xie, F. Wu, Y. Mei, Y. Hao, L. Li, R. Chen, *Adv. Mater.* **2022**, *34*, 2106897.
[71] N. Zhang, F. Cheng, J. Liu, L. Wang, X. Long, X. Liu, F. Li, J. Chen, *Nat.Commun* **2017**, *8*, 405.
[72] G. Lai, P. Ruan, X. Hu, B. Lu, S. Liang, Y. Tang, J. Zhou, *J. Mater. Chem. A* **2023**, *11*, 15211.
[73] W. Li, X. Gao, Z. Chen, R. Guo, G. Zou, H. Hou, W. Deng, X. Ji, J. Zhao, *Chem. Eng. J.* **2020**, *402*, 125509.
[74] G. Kresse, J. Furthmüller, *Matter Mater. Phys.* **1996**, *54*, 11169.
[75] J. P. Perdew, K. Burke, M. Ernzerhof, *Phys. Rev. Lett.* **1996**, *77*, 3865.